ADVANCED THEORY AND SIMULATIONS
www.advtheorysimul.com

Photoexcitation in Solids: First-Principles Quantum Simulations by Real-Time TDDFT

*Chao Lian, Mengxue Guan, Shiqi Hu, Jin Zhang, and Sheng Meng**

An efficient and state-of-the-art real-time time-dependent density functional theory (rt-TDDFT) method is presented, as implemented in the time-dependent ab initio package (TDAP), which aims at performing accurate simulations of the interaction between laser fields and solid-state materials. The combination of length-gauge and velocity-gauge electromagnetic field has extended the diversity of materials under consideration, ranging from low dimensional systems to periodic solids. Meanwhile, by employing a local basis presentation, systems of a large size are simulated for long electronic propagation time, with moderate computational cost while maintaining a relatively high accuracy. Non-perturbative phenomena in materials under a strong laser field and linear responses in a weak field can be simulated, either in the presence of ionic motions or not. Several quintessential works are introduced as examples for applications of this approach, including photoabsorption properties of armchair graphene nanoribbon, hole-transfer ultrafast dynamics between MoS_2/WS_2 interlayer heterojunction, laser-induced nonthermal melting of silicon, and high harmonic generation in monolayer MoS_2. The method demonstrates great potential for studying ultrafast electron-nuclear dynamics and nonequilibrium phenomena in a wide range of quantum systems.

1. Introduction

Real-time time-dependent density functional theory (rt-TDDFT) approaches, wherein the electron density is propagated in real time through numerical integration of the time-dependent Kohn–Sham (TDKS) equations, receive intensive interests recently in the research frontier of laser–matter interaction.[1,2] The rt-TDDFT methods could provide directly time-domain evolution of electronic wave functions together with ionic movements, representing a versatile way for real-time tracking of ultrafast dynamics and phenomena either in perturbative or non-perturbative regimes.[3–8] Therefore, it has been a unique ab initio quantum method applicable for the exploring of strong field physics beyond linear response theory, for instance, high harmonic generation [9,10] and ultrafast photoelectron emission.[11]

Recently, the scope of rt-TDDFT applications has greatly extended from treating isolated atomic and molecular systems to condensed phase materials. In most previous works, numerical implementations of rt-TDDFT that aim at handling solid materials were built on real-space grids,[12,13] including some well-known program packages such as OCTOPUS[9,14] and SALMON.[15,16] Real-time TDDFT has also been implemented in plane wave codes, for example, the ELK FP-LAPW[17] and FPSID,[18] whose encouraging results have shown the effectiveness of the rt-TDDFT approaches. However, if one is interested in high energy excitation that is on the energy scale of tens to hundreds of electron volts (eV), extremely dense real-space grids and high kinetic energy of plane waves are indispensable. Meanwhile, to describe a system with N_a atoms, 10^3 to $10^4 \times N_a$ real-space grids or plane waves have to be used, which makes the simulation of large-size systems impractical using computer resources available at the present stage. The above two factors will significantly increase the computational cost and in turn limit the practicability of the rt-TDDFT methods.

Here we introduce a real-time ab initio approach based on local atomic basis for simulating electron-nuclear dynamics under laser excited conditions. This approach has been successfully implemented in the time-dependent ab initio package (TDAP) within the framework of density functional theory (DFT) and time-dependent DFT (TDDFT).[19,20] We use local atomic basis sets and real-time propagation of wave functions for solving the time-dependent Kohn–Sham (TDKS) equations, which endows our approach several advantages over available approaches, as discussed below.

I. The adoption of overwhelmingly efficient atomic orbital basis sets, which are small in size (10 × Na) and fast in performance, enables the simulation of either periodic systems or a finite-sized supercell with a large vacuum space without heavy computing cost, while maintaining a relatively

Dr. C. Lian, M. Guan, S. Hu, J. Zhang, Prof. S. Meng
Beijing National Laboratory for Condensed Matter Physics
and Institute of Physics
Chinese Academy of Sciences
Beijing 100190, P. R. China
E-mail: smeng@iphy.ac.cn
M. Guan, S. Hu, J. Zhang
University of Chinese Academy of Sciences
Beijing 100049, P. R. China
S. Meng
Collaborative Innovation Center of Quantum Matter
Beijing 100871, P. R. China

DOI: 10.1002/adts.201800055

© 2018 WILEY-VCH Verlag GmbH & Co. KGaA, Weinheim

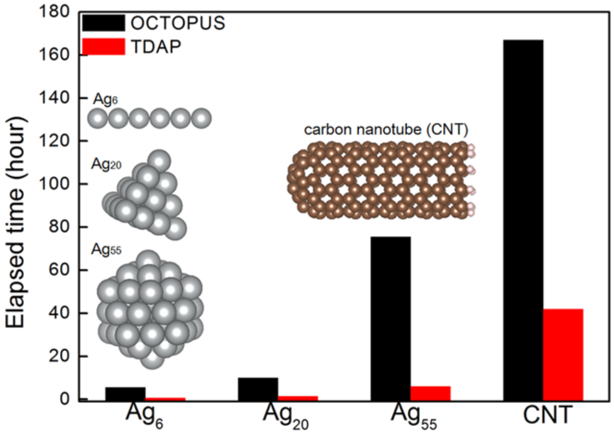

Figure 1. Elapsed computer time for evolving 40 fs electron dynamics in the time evolution calculation of Ag_6, Ag_{20}, Ag_{55}, and (10,0) carbon nanotube from OCTOPUS (black) and TDAP (red). The insets show the schematic atomic structures.

high accuracy. In **Figure 1**, we show the computational efficiency for calculating the optical response of metallic clusters Ag_6, Ag_{20}, Ag_{55}, as well as that for a complex semiconducting material, capped (10, 0) carbon nanotube (dangling bonds are saturated with hydrogen atoms, yielding a $C_{200}H_{10}$ tube) using the real-grid code OCTOPUS and the TDAP code. Within the real-space TDDFT code OCTOPUS, adiabatic local density approximation (ALDA) for the exchange correlation functional is used. The simulation zone is defined by assigning a sphere around each atom with a radius of 6.0 Å and a spacing of 0.2 Å between grid points. The Troullier–Martins pseudopotentials are used to represent the interaction between valence electrons and atomic core. To do the time integration of the electrons, approximated enforced time-reversal symmetry (AETRS) is used for evaluating the propagator. As for TDAP calculations, the same pseudopotentials, exchange correlation functional, and laser waveform have been used. Numerical atomic orbitals with double zeta polarization (DZP) are adopted as the basis set. Meanwhile, the first order Crank–Nicholson is used as the propagator. For the data shown in Figure 1, all the systems are evolved for the same time period (40 fs) in both OCTOPUS and TDAP by propagating Kohn–Sham wave functions. The efficiency can be extracted from the dependence of computer time on the system size by using the same number of message-passing-interface (MPI) processes and laser parameters. It is clear that the use of local atomic basis in the TDAP code can accelerate the simulation efficiency by four to ten times for these relatively small systems.

II. Electronic states localized near the atomic nucleus can be treated efficiently by employing the approach of linear combination of atomic orbitals (LCAO) approach. Thus, it is promising to realize simulations that focus on understanding the inner-shell excitations and to investigate electron dynamics on the femtosecond and sub-femtosecond time scale.[21]

III. Real-time excited state trajectories are achieved with many-electron density propagating self-consistently at every electronic and nuclear steps and forces calculated from mean-field theory, offering a direct microscopic picture on ultrafast dynamics of electrons and nuclei upon photoexcitation.

IV. Thanks to the development of the momentum (**k**) resolved rt-TDDFT algorithm, calculations of solids and surfaces can be performed by using a rather small unit cell, having reduced computational cost by several orders of magnitudes. Moreover, **k** resolved excitation dynamics are observed, showing the necessity and importance of the approach to reveal detailed mechanisms at the atomic level.

Our approach behaves well in treating quantum dynamics processes including photoabsorption, interface electron injection, electron-hole combination, structure phase transition, as well as high harmonic generation. The advantages of employing a real-time approach of TDDFT enable us to simulate quantum materials under strong ultra-short laser field beyond the perturbative theory, and nonequilibrium "hidden states," as well as exotic behaviors in a variety of degrees of freedom (electron, lattice, spin, ...).[22] At present, these studies are limited to the investigation of early stages (a few hundreds of femtosecond) of excited state dynamics due to the constraints of computer resources and the stability of algorithms. However, when there is branching in the electronic trajectories, our approach can address issues related to the mechanisms leading to the branch or decay. Efforts along this line are currently underway.

2. Methodology

For the simulation of periodic solid-state materials, the **k**-space resolution is most desired for the sake of revealing the nature of photoexcitation and for fast time evolution of complex electronic structures. An important advantage of using **k**-resolved rt-TDDFT is its computational efficiency. With many **k**-points sampling the reciprocal space, a relatively small simulation cell can be used to simulate quantum phenomena for a long time. Meanwhile, **k**-resolved algorithm introduces the important **k**-space resolution and a new degree of freedom, which is essential to describe key quantities and important physics in condensed matter materials such as time-dependent band structure, quasiparticles scattering, and valley dynamics. In other words, only rt-TDDFT with **k**-resolved sampling can provide essential information concerning their real-time evolution. From this point of view, we have successfully developed **k**-resolved rt-TDDFT algorithm based on local atomic basis sets. The main framework of **k**-resolved rt-TDDFT algorithm is inherited from an earlier single-Γ version of TDAP,[19] which is based on the SIESTA package.[23,24] **Figure 2** shows the flowchart of real-time excited state simulation at a given electronic step, which will be explicitly described in the following section.

2.1. Hamiltonian and Overlap Matrix

Adopting the periodic boundary conditions, the lattice vectors are denoted as $\mathbf{R}_s$ ($s = 1, 2, 3, \ldots, N$) and the atoms are denoted by index i in the unit cell located at positions $\mathbf{b}_i$, where N is truncated to form a finite supercell. A set of numerical

© 2018 WILEY-VCH Verlag GmbH & Co. KGaA, Weinheim

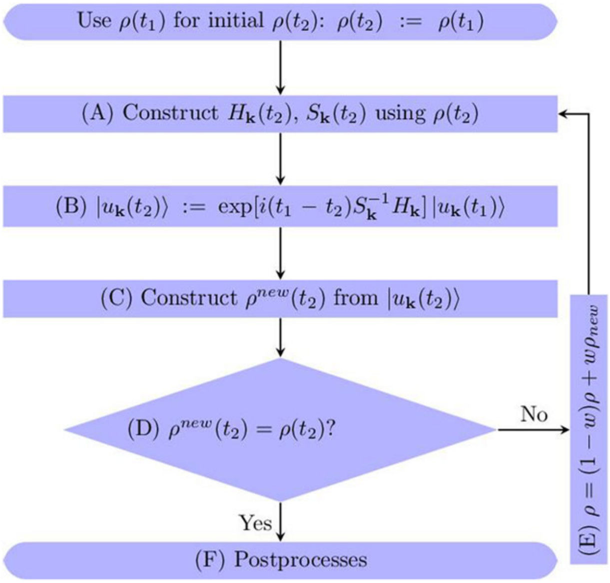

Figure 2. Flowchart of **k**-resolved algorithm for the evolution of electronic system. Here, $S_{\mathbf{k}}$ is the overlap matrix, $H_{\mathbf{k}}$ is the Hamiltonian matrix, and $u_{n\mathbf{k}}$ is the TDKS orbitals at **k**.

atomic-centered orbitals (NAOs) are associated with each atom, where α denotes both the orbital and angular quantum numbers of the atomic state, together with the multiple radial basis function ζ.[23] The local basis functions are numerical radial functions multiplied by spherical harmonics. The parameters for generating atomic basis sets we use here are default values generated by SIESTA, with well converged results.[23–26] For simplification, atomic units $\hbar = m_e = e = 1$ are used and only operators that explicitly dependent on t are denoted as $f(t)$ throughout this work unless specifically noted.

Overlap matrix $S_{\mathbf{k}}$ and Hamiltonian $H_{\mathbf{k}}$ at each $\mathbf{k}$ point are expressed with NAOs

$$S_{i\alpha,j\beta,\mathbf{k}} = \sum_s e^{-i\mathbf{k}\cdot\mathbf{R}_s} \left\langle \xi_{i\alpha}(\mathbf{r}+\mathbf{R}_s+\mathbf{b}_i) \middle| \, \xi_{j\beta}(\mathbf{r}+\mathbf{b}_j) \right\rangle \tag{1}$$

$$H_{i\alpha,j\beta,\mathbf{k}} = \sum_s e^{-i\mathbf{k}\cdot\mathbf{R}_s} \langle \xi_{i\alpha}(\mathbf{r}+\mathbf{R}_s+\mathbf{b}_i) \mid \hat{H} | \, \xi_{j\beta}(\mathbf{r}+\mathbf{b}_j) \rangle \tag{2}$$

where s is the index of ion, which sums over an auxiliary supercell. For periodic systems, the auxiliary supercell is needed to compute properly the matrix elements involving orbitals in different unit cells. The volume of auxiliary supercell is determined based on the criterion that the boundary is larger than the cutoff of the atomic orbitals. The widely used Monkhorst–Pack scheme for Brillouin zone integration is also adopted. The results are convergent with well tested mesh grid size. [23–27]

Here,

$$\hat{H} = \hat{T} + \sum V_I^{\mathrm{local}}(\mathbf{r}) + \sum V_I^{\mathrm{KB}} + V^{\mathrm{H}}(\mathbf{r}) + V^{\mathrm{XC}}(\mathbf{r}) + V^{\mathrm{ext}}(\mathbf{r}) \tag{3}$$

is the Hamiltonian operator, $\hat{T} = \frac{1}{2}\nabla_{\mathbf{r}}^2$ is the kinetic energy operator, V_I^{local} and V_I^{KB} are the local and Kleinman–Bylander parts of the pseudopotential of atom I, and V^{H}, V^{XC}, V^{Eext} are the Hartree, exchange-correlation (XC), and external electric field potential, respectively. At a given time t, the XC energy ($E_{\mathrm{xc}}(\rho(t))$) is only determined by the charge density $\rho(t)$. At each time step, the calculation of E_{xc} with the given $\rho(t)$ is carried out by the original SIESTA subroutines, in the same way as the processes in regular DFT calculation. Therefore, all functionals working in SIESTA (e.g., CA, PW92, PBE, revPBE, RPBE, PBEsol, KBM, WC, BLYP) are accessible in the current implementation, while the hybrid functionals have not been implemented because additional self-consistent processes for calculating the Hartree–Fock exchange term are needed. We note that the nonlocal part of the pseudopotential would also depend on the vector potential to preserve the gauge invariance. Details in the calculation of $\langle \xi_{i\alpha}(\mathbf{r}+\mathbf{R}_s+\mathbf{b}_i)|\hat{H}|\xi_{j\beta}(\mathbf{r}+\mathbf{b}_j)\rangle$ are described by Ordejón, et al.[24]

To simulate the interaction between laser field and various materials, time-dependent electric field $\mathbf{E}(t)$ is introduced to the Hamiltonian in two different scenarios: length gauge and vector gauge. Within length gauge, the effect of electric field $\mathbf{E}(t)$ is added via V^{ext},

$$V^{\mathrm{ext}}(\mathbf{r},t) = -\mathbf{E}(t)\cdot\mathbf{r} \tag{4}$$

In order to overcome the troubles that the transitional symmetry of Hamiltonian might be broken by the presence of $\mathbf{E}$, a sawtooth field along spatial direction $\mu \in x, y, z$ is used

$$E_\mu(\mathbf{r},t) = \begin{cases} E_\mu(t) & \varepsilon < x_\mu < L_\mu - \varepsilon \\ -E_\mu(t)L_\mu/2\varepsilon & -\varepsilon < x_\mu < +\varepsilon \end{cases} \tag{5}$$

in which L_μ is the length of unit cell along μ and $\varepsilon \to 0$. As a result, it is vital to make sure that charge density $\rho(x_\mu)$ must vanish in the region $-\varepsilon < x_\mu < +\varepsilon$. Otherwise, the energy will diverge for $-E_\mu(t)L_\mu/2\varepsilon \to \infty$. In this case, systems will be prelimited into a supercell with vacuum layers along μ,[8,28] which limits the approach to be applied only to finite systems.

To overcome the limitations mentioned above, the velocity gauge form for the TDKS equations suitable for infinite periodic systems is developed through a gauge transformation involving the vector potential for electromagnetic field,

$$A = -c\int E\,dt,\; E = -\frac{1}{c}\frac{\partial A}{\partial t} \tag{6}$$

yielding the velocity-gauge TDKS equation

$$H = \frac{1}{2m}(\hbar k - \frac{e}{c}A)^2 = \frac{1}{2m}(\hbar k + e\int E\,dt)^2 = \frac{\hbar^2}{2m}(k + k_A)^2 \tag{7}$$

$$k_A = \frac{e}{\hbar}\int E\,dt \tag{8}$$

It should be pointed out that periodic vector potentials are essential to describe accurate exchange-correlation effects of periodic systems. However, the necessary extension from scalar to vector potential has not yet been implemented. Moreover, the

© 2018 WILEY-VCH Verlag GmbH & Co. KGaA, Weinheim

shape of $\mathbf{E}(t)$ can be discretionarily tuned in either case, for example, assuming a Gaussian wave package

$$\mathbf{E}(t) = \mathbf{E}_0 \cos(2\pi f t + \phi) \exp\left[-\frac{(t-t_0)^2}{2\sigma^2}\right] \tag{9}$$

where f is the laser frequency, t_0 is the peak time, and ϕ is the auxiliary phase.

2.2. Time Propagation

With time-dependent Hamiltonian and overlap matrix, TDKS equations are solved to obtain $u_{n\mathbf{k}}(\mathbf{r}, t)$ from the data at the previous time step,

$$\left|u_{n\mathbf{k}}(\mathbf{r}, t_2)\right\rangle = \exp\left[-i\, S_{\mathbf{k}}^{-1}(t')\, H_{\mathbf{k}}(t')\Delta t\right] \left|u_{n\mathbf{k}}(\mathbf{r}, t_1)\right\rangle \tag{10}$$

where $u_{n\mathbf{k}}(\mathbf{r}, t) = \psi_{n\mathbf{k}}(\mathbf{r}, t)\exp(-i\mathbf{k}\cdot\mathbf{r})$ is the periodic part of Bloch function, and $\Delta t = t_2 - t_1$ is the length of time step, and $t' \approx (t_1 + t_2)/2$. Typically, Δt is quite small ($<$0.05 fs) and ion positions $\mathbf{b}_i$ barely change from t_1 to t_2, which ensure the rationality to take $S_{\mathbf{k}}(t') = S_{\mathbf{k}}(t_2)$ for evolving $S_{\mathbf{k}}(t)$ in Equation (1). However, $H_{\mathbf{k}}(t)$ may vary significantly due to the rapid evolution of electrons, two options are available,

$$H_{\mathbf{k}}(t') = H_{\mathbf{k}}(t_2) \tag{11}$$

$$H_{\mathbf{k}}(t') = \frac{1}{2} H_{\mathbf{k}}(t_2) + \frac{1}{2} H_{\mathbf{k}}(t_1) \tag{12}$$

As pointed out by Wang, et al. and Ren, et al.[29,30], Hamiltonian elements change approximately linearly within 0.2–0.5 fs. From this perspective, the latter is more accurate than the former with $\Delta t < 0.05$ fs. Nevertheless, these two scenarios yield almost the same results in practice.

Note that, when v-representativity is adopted for TDKS equations,[1] even though $u_{n\mathbf{k}}(\mathbf{r})(t_2)$ is not explicitly dependent on the other TDKS orbitals $u_{n'\mathbf{k}'}(\mathbf{r})(t_1)(n' \neq n$ or $\mathbf{k}' \neq \mathbf{k})$, interband scattering can be included for that $H_{\mathbf{k}}$ is determined by the total charge density, which is a weighted summation over all $\mathbf{k}$ points and all occupied orbitals. Numerically, the propagator $\exp(-i\, S_{\mathbf{k}}^{-1} H_{\mathbf{k}}\Delta t)$ in Equation (10) is expanded using the first order Crank–Nicholson scheme,

$$\left|u_{n\mathbf{k}}(\mathbf{r}, t_2)\right\rangle = \frac{1 - i\, S_{\mathbf{k}}^{-1} H_{\mathbf{k}}\Delta t/2}{1 + i\, S_{\mathbf{k}}^{-1} H_{\mathbf{k}}\Delta t/2} \left|u_{n\mathbf{k}}(\mathbf{r}, t_1)\right\rangle \tag{13}$$

Technically, calculation of Equation (13) is accelerated in two aspects: Firstly, ScaLAPACK is used for the parallel matrix inversion and multiplication. Secondly, $S_{\mathbf{k}}^{-1}$ is only updated when NAO positions $\mathbf{b}_i$ are changed to minimize the computer time used. Then, if ions are fixed, $S_{\mathbf{k}}^{-1}$ is computed only once at the first ionic step. Otherwise, $S_{\mathbf{k}}^{-1}(t_2)$ only need to be updated once for each ionic step.

2.3. Charge Density and Self-Consistency

With $u_{n\mathbf{k}}(\mathbf{r}, t_2)$ solved in Equation (10), the density matrix (DM) $\rho_{i\alpha,j\beta}(t_2)$ is computed accordingly as

$$\rho_{i\alpha,j\beta}(t_2) = \sum_n \sum_{\mathbf{k}} q_{n,\mathbf{k}} c^*_{n,i\alpha,\mathbf{k}}(t_2) c_{n,j\beta,\mathbf{k}}(t_2) \tag{14}$$

where $q_{n,\mathbf{k}}$ is electronic population of the band n at $\mathbf{k}$, $c_{n,j\beta,\mathbf{k}}(t_2)$ is the coefficient of $u_{n\mathbf{k}}(\mathbf{r}, t_2)$ in NAO basis,

$$u_{n\mathbf{k}}(\mathbf{r}, t_2) = \sum_{j\beta} c_{n,j\beta,\mathbf{k}}(t_2)\xi_{j\beta}(\mathbf{r}) \tag{15}$$

The self-consistent process[31] will substantially increase the numerical stability. In this case all criteria for convergence test developed in our code are compatible with those used in SIESTA, such as that based on the difference in the maximum element of DM, the difference in total energy, and the Harris energy difference. Here, we take the convergence criterion based on the difference in DM as an example. Convergence is reached when

$$\max\left\{\left|\rho^{\text{new}}_{i\alpha,j\beta} - \rho_{i\alpha,j\beta}\right|\right\} < \eta \tag{16}$$

where η is about 10^{-4}. If not, the linear mixing of DM is needed to generate the input DM for the next cycle ρ_{next}, instead of using ρ_{new} directly,

$$\rho = (1-w)\rho + w\rho_{\text{new}} \tag{17}$$

where the ρ is the input DM and ρ_{new} is the output DM, w is the mixing weight, usually $w = 0.1$–0.5.

2.4. Post-Processing

Once the self-consistency in charge density evolution is satisfied, post-processing such as the calculation of total energy, Hellmann–Feynman forces, ionic trajectory will be evoked. For instance, the forces acting on the ions can be calculated through the Hellmann–Feynman theorem:

$$\mathbf{F}_{\mathbf{R}_I} = \sum_i \langle\psi_i|\nabla_{\mathbf{R}_I} H|\psi_i\rangle \tag{18}$$

where $\mathbf{R}_I$ and $\mathbf{F}_{\mathbf{R}_I}$ are the position and force of Ith ion. With $\mathbf{R}_I$ and $\mathbf{F}_{\mathbf{R}_I}$, we invoke the Ehrenfest theorem for the equation of ionic motion:

$$M_I \frac{d^2\mathbf{R}_I}{dt^2} = \mathbf{F}_{\mathbf{R}_I} \tag{19}$$

which recovers Newton's second law of motion for the ionic degrees of freedom.

Then, only some unique methods for analysis are introduced as follows. First of all, the state-to-state transition probabilities can be calculated by[32]

$$P_{nn'\mathbf{k}} = |C_{nn'\mathbf{k}}|^2 = |\langle v_{n\mathbf{k}}|S_{\mathbf{k}}|u_{n'\mathbf{k}}\rangle|^2 \tag{20}$$

© 2018 WILEY-VCH Verlag GmbH & Co. KGaA, Weinheim

where $v_{n\mathbf{k}}$ is the adiabatic basis

$$H_{\mathbf{k}} \left|v_{n\mathbf{k}}(\mathbf{r})\right\rangle = E_{n\mathbf{k}} S_{\mathbf{k}} \left|v_{n\mathbf{k}}(\mathbf{r})\right\rangle \tag{21}$$

The population $q_{n\mathbf{k}}$ of adiabatic state $n\mathbf{k}$ is thus projected from TDKS orbitals as

$$q_{n\mathbf{k}} = \sum\nolimits_{n' \in n_{\mathbf{k},\mathrm{occ}}} q_{n'\mathbf{k}} P_{nn'\mathbf{k}} \tag{22}$$

$n_{\mathbf{k},occ}$ is occupied state at $\mathbf{k}$ point.

Technically, n loops over all adiabatic states, which has the same dimension N_o as NAOs. Assuming that N_{occ} is the number of occupied TDKS states, then the computational cost is up to $N_{\mathrm{occ}} O(N_o^2)$. The calculation is very time consuming, and parallel computation is thus essential. In the first place, diagonalization of $H_{\mathbf{k}}$ in Equation (21) is carried out by ScaLAPACK and all $v_{n\mathbf{k}}(\mathbf{r})$ are broadcasted to all nodes. Furthermore, the occupied TDKS orbitals $u_{n'\mathbf{k}}$ are distributed equally by all the computing nodes, and each node only evaluates Equation (20) with local TDKS orbitals.

Secondly, different response functions are employed. For finite-size structures, we calculate time-dependent dipole moment in the direction perpendicular to the vacuum layer,

$$\mathbf{D} = \int \rho(\mathbf{r})\mathbf{r}d\mathbf{r} \tag{23}$$

where $\rho(\mathbf{r})$ is charge density. However, for periodic systems, dipole is ill-defined and the time-dependent current is computed,

$$\mathbf{j} = -i\frac{e\hbar}{m}\sum_{n}\left[\langle u_{n\mathbf{k}}|\nabla|u_{n\mathbf{k}}\rangle - \langle u_{n\mathbf{k}}^{*}|\nabla|u_{n\mathbf{k}}^{*}\rangle\right] \tag{24}$$

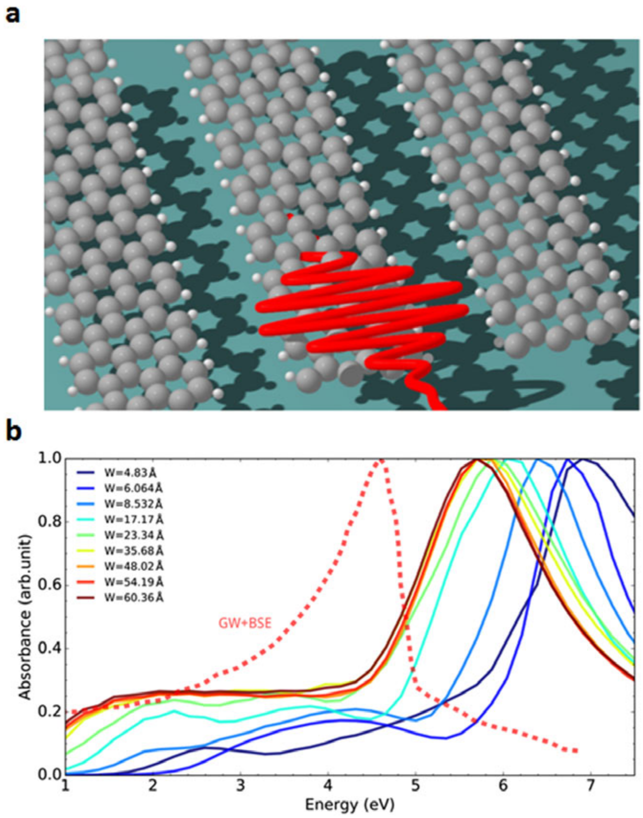

Figure 3. a) A schematic showing AGNRs under an external electric field polarized along the ribbon width direction. b) Optical absorption spectra of AGNRs in different widths.

3. Some Examples Toward Simulating Realistic Systems

We intent to develop our code focusing on light–matter interactions as main application fields. Light-induced electron and phonon dynamics can be handled efficiently for isolated and periodic systems. Up to now, we have employed the real-time local basis TDDFT approach to investigate ultrafast dynamics in some prototypical systems for important applications. In the following section, several quintessential examples are introduced in detail.

3.1. Photoabsorption Spectra and Electron Dynamics in Graphene Nanoribbons

Firstly, we use the present rt-TDDFT method to calculate the photoabsorption properties of armchair graphene nanoribbons (AGNRs) and to monitor the excitation mode with the $\mathbf{k}$-point resolution. For AGNRs,[33,34] there is a vacuum layer along the in-plane direction perpendicular to the ribbon edge, and the laser field in the length gauge is used. The intensity of optical absorption along $\mu \in (x, y, z)$ direction can be expressed as the imaginary part of the dielectric function

$$S_{\mu}(\omega) = \mathrm{Im}\left\{\alpha_{\mu,\mu}(\omega)\right\} \tag{25}$$

where $\alpha_{\mu,\upsilon}$ characterizes the response of dipole moment $P_{\mu}(\omega)$ to the electric field $E_{\upsilon}(\omega)$ in the frequency domain,

$$P_{\mu}(\omega) = \alpha_{\mu,\upsilon}(\omega) E_{\upsilon}(\omega) \tag{26}$$

In rt-TDDFT calculations, we apply the electric field $E_{\upsilon}(t)$ to obtain the dipole moment $P_{\mu}(t)$ in time domain. Then the Fourier transform is performed to obtain the polarizability in the frequency domain,

$$\alpha_{\mu,\upsilon}(\omega) = \frac{\int P_{\mu}(t)\exp(i\omega t)dt}{\int E_{\upsilon}(t)\exp(i\omega t)dt} \tag{27}$$

where $E_{\upsilon}(t)$ is chosen as a Heaviside step function,

$$E_{\upsilon}^{\theta}(t) = E_{\upsilon}^{0}\left[1-\theta(t)\right] = \begin{cases} E_{\upsilon}^{0}(t) & t \le 0 \\ 0 & t > 0 \end{cases} \tag{28}$$

In the present work, $E_{\upsilon}(t)$ is applied along the direction perpendicular to the ribbon edge (**Figure 3**a). The resonance absorption spectrum $S(\omega)$ is obtained in a board energy range from infrared to ultraviolet (1–7 eV). For AGNRs with different widths, the absorption spectra are shown in Figure 3b. We observe two kinds of resonance peaks implying different excitation modes: the visible and the higher energy light excitation modes, whose

© 2018 WILEY-VCH Verlag GmbH & Co. KGaA, Weinheim

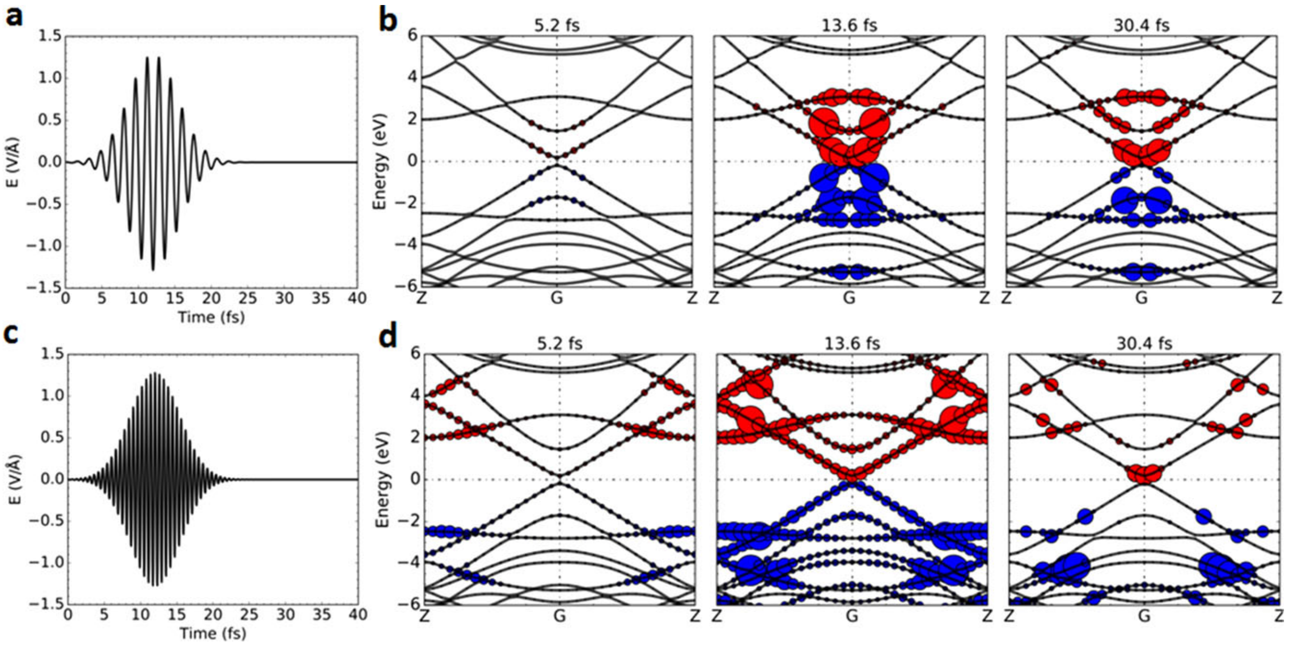

Figure 4. Momentum resolved excitation in the graphene nanoribbon (width $W = 4.83$ Å) under two laser excitation modes. a) Profile of applied electric field, where the frequency ω is set as 2.59 eV. b) Snapshot of electron population distribution at three selected moments. c,d) Same as (a) and (b) but for a higher laser frequency with $\omega = 6.90$ eV.

peak position are around 1–4 eV and 6–7 eV, respectively. An obvious redshift and a clear convergence tendency occur for both of two modes with the increasing width of ribbon (W), which are in considerable agreement with the experimental data.[35,36] For the higher energy excitation mode, the monotonous redshift (from 6.7 eV for $W = 6.064$ Å to 5.6 eV for $W = 60.36$ Å) can be extrapolated to a value close to the result on the $\pi-\pi$ band transition in monolayer graphene (MG) calculated by GW plus Bethe–Salpeter equation (red dash line in Figure 3b).[37] It implies that the evolution corresponds to the transition from ID ANGRs band structures to 2D graphene band structures as the ribbon width increases. However, for the mode in visible region, the peaks will be broadened into an uniform absorption background when the ribbon width come to infinite, consistent with the existence of the constant absorption in monolayer graphene (light absorption $\pi\alpha = 2.3\%$).[38] In addition, the peak locations remain the same under the impulse field strength E_0 ranging from 0.25 to 2.5 VÅ^{-1}, implying these excitation modes are robust.

To gain deeper information on the excitation dynamics, we show the **k** resolved snapshots of electron population distribution during the visible light (**Figure 4**a) and high energy excitation (Figure 4c). Red (blue) dots in Figure 4b,d denote the increase (decrease) of electron occupation, and the size represents the population of excited electrons and holes. For visible light mode, the population is mainly distributed on some special **k** points, showing a feature of single electron-hole excitations. While for high energy mode, the excitation is distributed on almost all the **k** points, showing a collective excitation behavior. These results demonstrate that the present approach is accurate and efficient in calculating and analyzing optical properties in complex nanostructures.

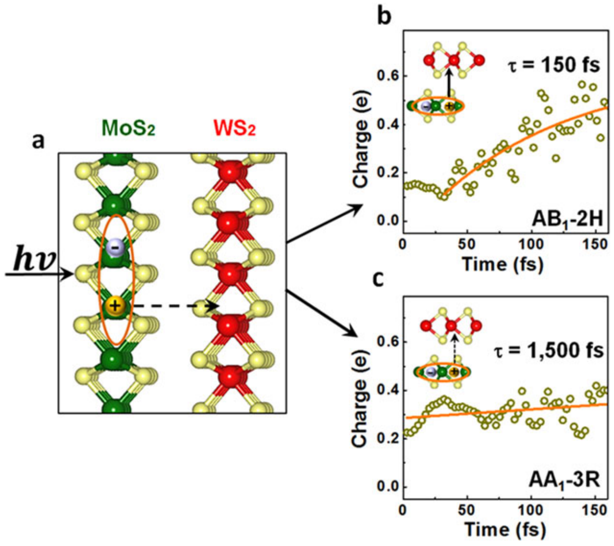

Figure 5. Ultrafast charge transfer in MoS_2/WS_2 bilayer. a) Side view of MoS_2/WS_2 bilayer. Green, red, yellow spheres represent Mo, W, and S atoms, respectively. b,c) Hole transfer dynamics for MoS_2/WS_2 in two stacking modes. The transfer lifetime is fitted by an exponential function. The insets show the schematic atomic structures.

3.2. Ultrafast Charge Dynamics in MoS_2/WS_2 Heterojunction

Laser-induced interlayer ultrafast charge transfer plays a very important role in determining both the speed and efficiency of charge separation, which provides a new platform for optoelectronic and photovoltaic applications.[39,40] Here, we use a model MoS_2/WS_2 bilayer system (**Figure 5**a) as an example to show how the local-basis rt-TDDFT method can be employed to monitor the electronic dynamics in such a van der Waals heterostructure.[41] By choosing the photon energy to match that of MoS_2 bandgap, electrons will be excited from the selected valence band and holes are created in the MoS_2 layer. Afterward, the holes will transfer into the neighboring WS_2 layer in the heterojunction. The time evolution of interlayer charge transfer is simulated by simultaneously solving the time-dependent Kohn–Sham equation and Newtonian motion of ions.

Our results show that a slight interlayer geometry modulation of twisting, translation, or spacing can tune charge transfer dynamics very efficiently. As displayed in Figure 5b,c, both AB_1-2H and AA_1-3R are the stable stacking configurations in MoS_2/WS_2 bilayer with the same interlayer distance (6.3 Å).[42,43] However, to form the other configuration, one layer in the bilayer rotates by an angle of π. We fit the time evolution data with an exponential equation $\chi = a + b \times \exp(-t/\tau)$, where τ is the charge transfer life time and χ is the hole (electron) density on the WS_2 orbitals at different times after photoexcitation. As marked in Figure 5b,c, τ_{AB_1} and τ_{AA_1} are around 100 fs and 1000 fs, respectively, differing by an order of magnitude in charge transfer timescale, despite that the two configurations have a similar interlayer binding energy.

Further analysis demonstrates that the interlayer charge transfer is only related to the coupling between some specific interlayer states, in this case is the one between $|-2\rangle$ and $|-1\rangle$ states at K point in the Brillouin zone. The dipole transition matrix elements $M = \langle -2|\hat{Z}|-1\rangle$ is used to evaluate the coupling strength between the two states, where $\hat{Z}$ is the position operator along the vertical direction normal to the MX_2 plane. We found $M_{AB_1} \gg M_{AA_1}$ and the detailed analysis further reveals that $1/\tau$ is exponentially dependent on M, therefore, the distinct charge transfer dynamics in above two stacking modes is understandable. Based on these findings, one could utilize various methods to modulate the interlayer geometry, and therefore the charge transfer quantum dynamics can be controlled. This study will facilitate future applications of 2D heterostructures in novel optoelectronic and light harvesting devices.

3.3. Laser-Induced Nonthermal Melting

Laser excitation generates ultrafast phenomena and unique condensed phases of matter.[44] A popular example is ultrafast melting. Melting within a timescale of less than a picosecond upon photoexcitation has been ubiquitously observed in a wide range of semiconductors,[45–47] and, most recently, in 2D materials such as $TiSe_2$[48] and TaS_2.[49] Despite extensive experimental and theoretical investigations in the past four decades, the atomistic mechanism of ultrafast melting remains controversial. Initiated by this situation, we simulate laser melting of Si under experimental conditions as shown in **Figure 6**.[46,50] Our simulations, by combining local basis rt-TDDFT and molecular dynamics (MD) approaches, explicitly show that ultrafast laser melting could occur at a temperature (600 K) significantly below the equilibrium thermal melting temperature (≈1700 K for Si), thus confirming the nonthermal and nonequilibrium nature of laser melting for the first time.

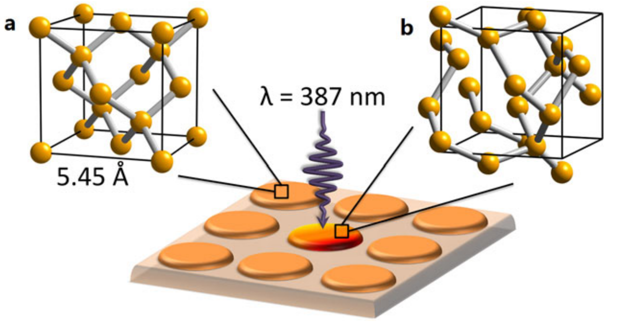

Figure 6. Schematic showing the atomic structure of silicon crystal a) before and b) after laser melting.

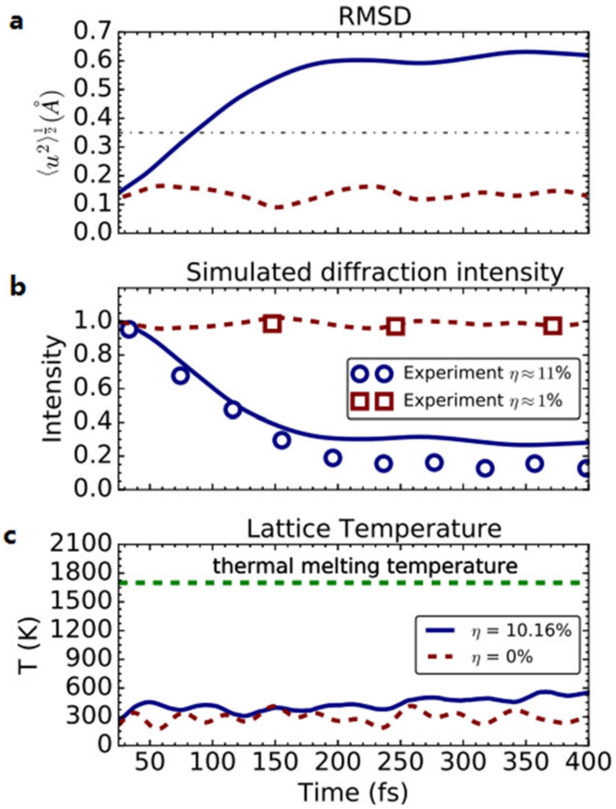

Figure 7. a) RMSD as a function of time. b) Simulated and experimental electron diffraction intensity of (220) reflection as a function of time. Experimental data (time rescaled by a factor of 0.33) are taken from ref. [43]. c) Ionic temperature as a function of time.

We adopt the Lindemann criterion for judging the melting of crystal lattice: silicon melts when its root-mean-square displacement (RMSD) $<u^2(t)>^{\frac{1}{2}}$ is larger than the critical value $R_c = 0.35$ Å (15% of Si–Si bond length).[51] The RMSDs with and without laser irradiation are shown in **Figure 7**a. Here we use the percentage of valence electrons pumped to conduction bands to denote the laser intensity η. The maximum RMSD without laser ($\eta = 0\%$) reaches only half of R_c. However, the RMSD with laser intensity $\eta = 10.16\%$ crosses the R_c within 100 fs and keeps increasing to about 0.6 Å at 400 fs, showing an evident ultrafast melting behavior.

© 2018 WILEY-VCH Verlag GmbH & Co. KGaA, Weinheim

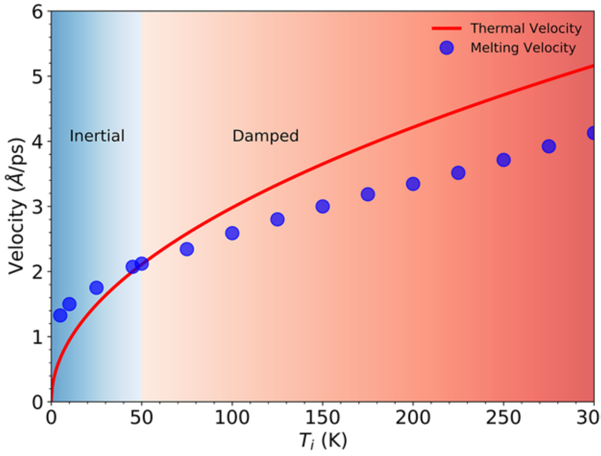

Figure 8. The melting velocity v_m (blue dots) and thermal velocity v_t (red line) as a function of ionic temperature.

The RMSD is directly connected to diffraction intensity $I(t)$ through the Debye–Waller formula:

$$I(t) = \exp\left[-Q^2 < u^2(t) > /3\right] \tag{29}$$

where Q is the reciprocal lattice vector of the probed reflection, $< u^2(t) >$ is the mean square displacement, that is, the square of RMSD. We simulate the $I_{\eta=10.16\%}(t)$ and $I_{\eta=0\%}(t)$ for the (220) reflection (Figure 7b). The features of the experimental data and our simulations are almost identical. The $I_{\eta=11\%}(t)$ decreases to 0.2 after melting in both the experiment and our simulation, while without laser, both the simulated and experimental curves show no drift but an oscillation around 0.95. It demonstrates that our simulation captures the most important features of nonthermal melting observed in experiment. The only difference is that in our simulation, the melting speed is even faster, possibly because of the small supercell size used in the simulation and other complications in experiment including surface effects and a large pulse width used (200 fs). We note that during the melting, the crystal lattice remains cold ($T < 600$ K; Figure 7c), revealing an intrinsic nonthermal melting.

The plasma annealing (PA) mechanism,[52] that is, plasma-induced bond weakening, seems to work well to explain the above results. The conventional PA model assumes that laser energy retains in the electronic subsystem, thus ultrafast melting is purely an electronic effect. However, we show that the PA is insufficient to fully understand ultrafast melting. The electron–phonon (el–ph) energy transfer is important but neglected in PA. During melting, the loss in ion kinetic energy is compensated by the energy transfer from electrons to ions via el–pl scattering. The el–ph energy transfer leads to peculiar phenomena distinct from what PA predicts. Inertial dynamics, namely melting with a constant ion velocity no less than average thermal velocity, is experimentally observed,[53] a direct evidence of el–ph energy transfer. The inertial dynamics dictates $v_\mathrm{m} \geq v_\mathrm{t}$, where v_m is the melting velocity $v_\mathrm{m} = \Delta < u^2(t) >^{\frac{1}{2}} / \Delta t$, and v_t is thermal velocity of ions $v_\mathrm{t} = \sqrt{3k_B T/M}$ (M is the atomic mass). Inertial dynamics is nicely reproduced in our simulations. The melting velocity v_m and thermal velocity v_t are shown in **Figure 8**. At an initial ion temperature similar to experiment $T_i = 300$ K, $v_\mathrm{m} < v_\mathrm{t}$ shows a damped melting, consistent with the experiment.[46] It can be explained by melting under a perturbed potential energy surface (PES). However, when T_i decreases to a critical temperature $T_\mathrm{c} = 50$ K, there exists a crossover between v_m and v_t. Below T_c, the inertial even accelerated melting dynamics is observed.

In PA model, upon laser excitation, ions either maintain their thermal velocity v_t (for flattened PES) or have a velocity smaller than v_t (for perturbed PES with a barrier) during melting, since ionic kinetic energy is consumed to overcome the melting barrier. This contradicts with the crossover between damped and inertial dynamics observed in our simulation and experiment. We suggest that laser-induced el–ph energy transfer, dominant at low temperatures, is the key for the observed inertial dynamics.

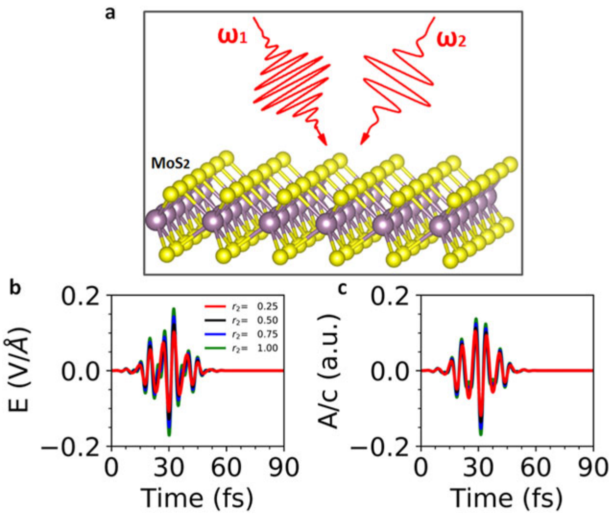

Figure 9. a) Schematic showing high harmonic generation under two-color fields. b) The electric field, and c) the vector potential of four representative laser pulses with different relative ratios.

3.4. High Harmonic Generation

Strong field laser excitation of solids can produce extremely nonlinear electronic and optical behaviors. One of the most fundamental and prominent aspects of nonlinear optics is higher-order harmonic generation (HHG) in condensed matter systems,[54–56] which is both a source of fundamental insight into electron motion and a promising new method to realize compact ultraviolet and ultrafast light sources. However, applications of the HHG are restricted by the low conversion efficiency, so enhancing the yield of HHG becomes a valuable project. In our work, two-color field is used to control the electron dynamic processes to enhance HHG intensity in monolayer $\mathrm{MoS_2}$, as shown in **Figure 9**a. The interaction of laser with $\mathrm{MoS_2}$ is calculated by solving the TDKS equation (Equation (6)) in velocity gauge and the two-color laser field is expressed to be a Gaussian envelop function:

$$\begin{aligned} E(t) &= \left\{E_1 \sin(\omega_1 t + \varphi_1) + E_2 \sin(\omega_2 t + \varphi_2)\right\} \\ &\quad \times \exp\left[-(t - t_0)^2/2\sigma^2\right] \qquad (30) \\ r_2 &= E_2/E_1 \end{aligned}$$

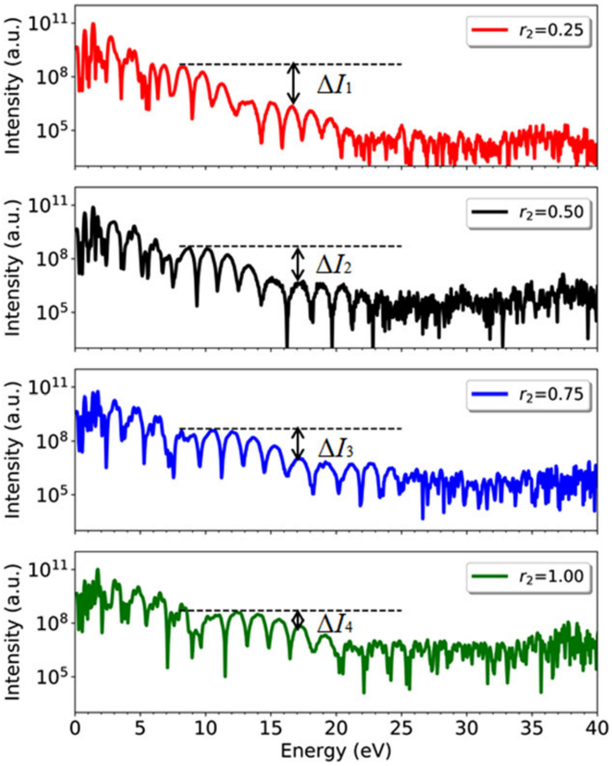

Figure 10. HHG spectra in the two-color fields with different relative intensity. The length of arrows shows intensity differences ΔI_i between the benchmark (black dashed line) and higher order harmonics, in this case, $\Delta I_1 > \Delta I_2 > \Delta I_3 > \Delta I_4$, which means that harmonic yields can be enhanced by properly-tuned two-color fields.

Here, E_i, φ_i, and ω_i $(i = 1, 2)$ are peak electric field, phase, and frequency, respectively. The relative ratio of the two laser pulse intensities is represent by r_2. In our simulation, linearly polarized laser is applied along the zigzag direction of monolayer MoS_2 with $E_1 = 0.07$ VÅ^{-1}, $\omega_2 = 1.5\omega_1 = 1/2 E_{\text{gap}}$ ($E_g = 1.94\,eV$), $\varphi_i = 0$, the pulse peak time $t_0 = 30$ fs while the half width is chosen to be $\sigma = 8.5$ fs. In Figure 9b,c, four representative laser pulses with different r_2 are displayed. Once the time-dependent current $J(t)$ is available via Equations (7) and (24), HHG spectrum can be accessed through Fourier transformation,

$$I(\omega) = \left| \int_0^T \omega^2 J(t) \exp(-i\omega t) dt \right|^2 \tag{31}$$

The corresponding HHG spectra are displayed in **Figure 10**. It is clear that the HHG spectrum is very sensitive to the participation of the second laser pulse. More precisely, when the peak intensity of the laser changes by only 40%, the yield of the high order harmonic can be increased by 10–100 times in the energy range of E > 10 eV. Meanwhile, by simply controlling the amplitude ratio of the second beam to the first one, the cutoff of the plateau region can be further extended, showing the possibility to generate isolated attosecond pulses.[57,58] The phenomena can be attributed to the fact that larger vector potentials are obtained when increasing r_2 coherently. A larger magnitude of the vector potential will increase electron transition probabilities from valence bands to conduction bands. More electrons would be excited and travel a larger fraction of the momentum space, thus leading to a high intensity in the HHG spectrum.

4. Conclusion

In summary, we present an efficient real-time TDDFT approach for large scale accurate simulations of excited state dynamics. Both length-gauge and velocity-gauge electromagnetic field have been implemented using numerical atomic orbitals as basis, ensuring the flexibility and credibility to apply this method to various laser-induced phenomena in diverse systems including solids, interfaces, and low-dimensional materials. Furthermore, recently developed momentum resolved algorithm provides the possibility to treat these systems with a small simulation cell, which significantly reduces the formidable computational cost of conventional rt-TDDFT simulations. We show several quintessential examples, including the photoabsorption properties of graphene nanoribbons, ultrafast charge transfer in MoS_2/WS_2 heterojunction, nonthermal melting of silicon, as well as high harmonic generation from monolayer MoS_2. Most of these applications represent a new prospect in their respective areas. We expect that the present approach could be extended to broader fields and become part of the standard tools for physicists, chemists, and materials scientists who are interested in laser–matter interactions.

Supporting Information

Supporting Information is available from the Wiley Online Library or from the author.

Acknowledgements

C.L. and M.G. contributed equally to this work. This work is supported by MOST (grants 2016YFA0300902 and 2015CB921001), NSFC (grants 11774396 and 11474328), and CAS (XDB07030100).

Conflict of Interest

The authors declare no conflict of interest.

Keywords

k-resolved algorithm, length and velocity-gauge, local atomic basis, real-time TDDFT

Published online:

---

[1] E. Runge, E. K. Gross, *Phys. Rev. Lett.* **1984**, *52*, 997.
[2] C. A. Ullrich, *Time-Dependent Density-Functional Theory: Concepts and Applications*, Oxford University Press, Oxford **2011**.
[3] S. Sato, K. Yabana, Y. Shinohara, T. Otobe, K. M. Lee, G. Bertsch, *Phys. Rev. B* **2015**, *92*, 205413.

© 2018 WILEY-VCH Verlag GmbH & Co. KGaA, Weinheim

[4] D. Sánchez-Portal, E. Hernandez, *Phys. Rev. B* **2002**, *66*, 235415.
[5] Y. Takimoto, F. Vila, J. Rehr, *J. Chem. Phys.* **2007**, *127*, 154114.
[6] K. Lopata, N. Govind, *J. Chem. Theory Comput.* **2011**, *7*, 1344.
[7] A. Castro, J. Werschnik, E. K. Gross, *Phys. Rev. Lett.* **2012**, *109*, 153603.
[8] K. Yabana, T. Sugiyama, Y. Shinohara, T. Otobe, G. Bertsch, *Phys. Rev. B* **2012**, *85*, 045134.
[9] N. Tancogne-Dejean, O. D. Mucke, F. X. Kartner, A. Rubio, *Phys. Rev. Lett.* **2017**, *118*, 087403.
[10] T. T. N. Yoshikawa, K. Tanaka, *Science* **2017**, *356*, 736.
[11] U. De Giovannini, D. Varsano, M. A. L. Marques, H. Appel, E. K. U. Gross, A. Rubio, *Phys. Rev. A* **2012**, *85*, 062515.
[12] X. Andrade, D. Strubbe, U. De Giovannini, A. H. Larsen, M. J. Oliveira, J. Alberdi-Rodriguez, A. Varas, I. Theophilou, N. Helbig, M. J. Verstraete, *Phys. Chem. Chem. Phys.* **2015**, *17*, 31371.
[13] S. A. Sato, K. Yabana, *J. Adv. Simulat. Sci. Eng.* **2014**, *1*, 98.
[14] X. Andrade, J. Alberdi-Rodriguez, D. A. Strubbe, M. J. Oliveira, F. Nogueira, A. Castro, J. Muguerza, A. Arruabarrena, S. G. Louie, A. Aspuru-Guzik, *J. Phys. Condens. Matter* **2012**, *24*, 233202.
[15] M. Noda, S. A. Sato, Y. Hirokawa, M. Uemoto, T. Takeuchi, S. Yamada, A. Yamada, Y. Shinohara, M. Yamaguchi, K. Iida, *arXiv preprint arXiv:1804.01404,* **2018**.
[16] X.-M. Tong, G. Wachter, S. A. Sato, C. Lemell, K. Yabana, J. Burgdörfer, *Phys. Rev. A* **2015**, *92*, 043422.
[17] K. Dewhurst, S. Sharma, L. Nordstrom, F. Cricchio, F. Bultmark, H. Gross, C. Ambrosch-Draxl, C. Persson, C. Brouder, R. Armiento, ELK, http://elk.sourceforge.net (accessed: May 2018).
[18] O. Sugino, Y. Miyamoto, *Phys. Rev. B* **1999**, *59*, 2579.
[19] S. Meng, E. Kaxiras, *J. Chem. Phys.* **2008**, *129*, 054110.
[20] W. Ma, J. Zhang, L. Yan, Y. Jiao, Y. Gao, S. Meng, *Comp. Mater. Sci.* **2016**, *112*, 478.
[21] C. Pemmaraju, F. Vila, J. Kas, S. Sato, J. Rehr, K. Yabana, D. Prendergast, *Comp. Phys. Comm.*, **2018**, *226*, 30.
[22] L. Stojchevska, I. Vaskivskyi, T. Mertelj, P. Kusar, D. Svetin, S. Brazovskii, D. Mihailovic, *Science* **2014**, *344*, 177.
[23] J. M. Soler, E. Artacho, J. D. Gale, A. García, J. Junquera, P. Ordejón, D. Sánchez-Portal, *J. Phys. Condens. Matter* **2002**, *14*, 2745.
[24] P. Ordejón, E. Artacho, J. M. Soler, *Phys. Rev. B* **1996**, *53*, R10441.
[25] J. Junquera, Ó. Paz, D. Sánchez-Portal, E. Artacho, *Phys. Rev. B* **2001**, *64*, 235111.
[26] F. Xu, H. Yu, A. Sadrzadeh, B. I. Yakobson, *Nano Lett.* **2015**, *16*, 34.
[27] M. E. Z. Michoff, J. Ribas-Arino, D. Marx, *Phys. Rev. Lett.* **2015**, *114*, 075501.
[28] K. Yabana, T. Nakatsukasa, J. I. Iwata, G. Bertsch, *Phys. Status Solidi B* **2006**, *243*, 1121.
[29] Z. Wang, S.-S. Li, L.-W. Wang, *Phys. Rev. Lett.* **2015**, *114*, 063004.
[30] J. Ren, N. Vukmirović, L.-W. Wang, *Phys. Rev. B* **2013**, *87*, 205117.
[31] J. Ren, E. Kaxiras, S. Meng, *Mol. Phys.* **2010**, *108*, 1829.
[32] N. Rohringer, S. Peter, J. Burgdörfer, *Phys. Rev. A* **2006**, *74*, 042512.
[33] Y.-W. Son, M. L. Cohen, S. G. Louie, *Phys. Rev. Lett.* **2006**, *97*, 216803.
[34] L. Yang, C.-H. Park, Y.-W. Son, M. L. Cohen, S. G. Louie, *Phys. Rev. Lett.* **2007**, *99*, 186801.
[35] H. Yan, X. Li, B. Chandra, G. Tulevski, Y. Wu, M. Freitag, W. Zhu, P. Avouris, F. Xia, *Nature Nanotech.* **2012**, *7*, 330.
[36] L. Ju, B. Geng, J. Horng, C. Girit, M. Martin, Z. Hao, H. A. Bechtel, X. Liang, A. Zettl, Y. R. Shen, *Nature Nanotech.* **2011**, *6*, 630.
[37] L. Yang, J. Deslippe, C.-H. Park, M. L. Cohen, S. G. Louie, *Phys. Rev. Lett.* **2009**, *103*, 186802.
[38] C. V. Gomez, M. Pisarra, M. Gravina, J. M. Pitarke, A. Sindona, *Phys. Rev. Lett.* **2016**, *117*, 116801.
[39] S. M. Falke, C. A. Rozzi, D. Brida, M. Maiuri, M. Amato, E. Sommer, A. De Sio, A. Rubio, G. Cerullo, E. Molinari, *Science* **2014**, *344*, 1001.
[40] C. A. Rozzi, S. M. Falke, N. Spallanzani, A. Rubio, E. Molinari, D. Brida, M. Maiuri, G. Cerullo, H. Schramm, J. Christoffers, *Nat. Commun.* **2013**, *4*, 1602.
[41] J. Zhang, H. Hong, C. Lian, W. Ma, X. Xu, X. Zhou, H. Fu, K. Liu, S. Meng, *Adv. Sci.* **2017**, *4*, 1700086.
[42] A. M. van Der Zande, J. Kunstmann, A. Chernikov, D. A. Chenet, Y. You, X. Zhang, P. Y. Huang, T. C. Berkelbach, L. Wang, F. Zhang, *Nano Lett.* **2014**, *14*, 3869.
[43] K. Liu, L. Zhang, T. Cao, C. Jin, D. Qiu, Q. Zhou, A. Zettl, P. Yang, S. G. Louie, F. Wang, *Nat. Commun.* **2014**, *5*, 4966.
[44] K. K. Ostrikov, F. Beg, A. Ng, *Rev. Mod. Phys.* **2016**, *88*, 011001.
[45] C. Shank, R. Yen, C. Hirlimann, *Phys. Rev. Lett.* **1983**, *50*, 454.
[46] M. Harb, R. Ernstorfer, C. T. Hebeisen, G. Sciaini, W. Peng, T. Dartigalongue, M. A. Eriksson, M. G. Lagally, S. G. Kruglik, R. D. Miller, *Phys. Rev. Lett.* **2008**, *100*, 155504.
[47] K. Sokolowski-Tinten, C. Blome, C. Dietrich, A. Tarasevitch, M. H. Von Hoegen, D. von der Linde, A. Cavalleri, J. Squier, M. Kammler, *Phys. Rev. Lett.* **2001**, *87*, 225701.
[48] M. Porer, U. Leierseder, J.-M. Ménard, H. Dachraoui, L. Mouchliadis, I. Perakis, U. Heinzmann, J. Demsar, K. Rossnagel, R. Huber, *Nature Mater.* **2014**, *13*, 857.
[49] S. Hellmann, M. Beye, C. Sohrt, T. Rohwer, F. Sorgenfrei, H. Redlin, M. Kalläne, M. Marczynski-Bühlow, F. Hennies, M. Bauer, *Phys. Rev. Lett.* **2010**, *105*, 187401.
[50] C. Lian, S. Zhang, S. Meng, *Phys. Rev. B* **2016**, *94*, 184310.
[51] E. S. Zijlstra, A. Kalitsov, T. Zier, M. E. Garcia, *Phy. Rev. X* **2013**, *3*, 011005.
[52] J. Van Vechten, R. Tsu, F. Saris, D. Hoonhout, *Phys. Lett. A* **1979**, *74*, 417.
[53] A. M. Lindenberg, J. Larsson, K. Sokolowski-Tinten, K. Gaffney, C. Blome, O. Synnergren, J. Sheppard, C. Caleman, A. MacPhee, D. Weinstein, *Science* **2005**, *308*, 392.
[54] G. Ndabashimiye, S. Ghimire, M. Wu, D. A. Browne, K. J. Schafer, M. B. Gaarde, D. A. Reis, *Nature* **2016**, *534*, 520.
[55] G. Vampa, T. J. Hammond, N. Thire, B. E. Schmidt, F. Legare, C. R. McDonald, T. Brabec, P. B. Corkum, *Nature* **2015**, *522*, 462.
[56] H. Liu, Y. Li, Y. S. You, S. Ghimire, T. F. Heinz, D. A. Reis, *Nature Phys.* **2016**, *13*, 262.
[57] J.-B. Li, X. Zhang, S.-J. Yue, H.-M. Wu, B.-T. Hu, H.-C. Du, *Opt. Express.* **2017**, *25*, 18603.
[58] A. D. Shiner, C. Trallero-Herrero, N. Kajumba, H. C. Bandulet, D. Comtois, F. Legare, M. Giguere, J. C. Kieffer, P. B. Corkum, D. M. Villeneuve, *Phys. Rev. Lett.* **2009**, *103*, 073902.

© 2018 WILEY-VCH Verlag GmbH & Co. KGaA, Weinheim